Numerical investigation on effects of fringing reefs on low-frequency oscillations within a harbor

Junliang Gao[1, 2], Xiaojun Zhou[1], Li Zhou[1 *], Jun Zang[2], Hongzhou Chen[3]

1. School of Naval Architecture and Ocean Engineering, Jiangsu University of Science and Technology, Zhenjiang 212003, China

2. Research Unit for Water, Environment and Infrastructure Resilience (WEIR), Department of Architecture and Civil Engineering, University of Bath, BA2 7AY, U.K.

3. School of Civil Engineering and Architecture, Northeast Electric Power University, Jilin, 132012, China

Abstract

The low-frequency (LF) oscillations inside an elongated rectangular harbor near the offshore fringing reef excited by bi-chromatic short wave groups are simulated using a fully nonlinear Boussinesq model. Based on a LF wave analysis procedure, effects of reef-face slope and reef ridge on the maximum LF wave amplitude, the free and the bound LF waves and their relative components inside the harbor are investigated systematically under the conditions of the 2nd to the 5th modes and wave breaking occurring over the reef. Results show that the variation trends of the maximum LF wave amplitude and the free LF wave amplitude with respect to the reef-face slope are almost identical with each other for all the four modes studied in this paper, no matter whether the reef ridge exists or not. For the 4th and 5th modes, the reef ridge has obvious influences on the LF waves inside the harbor. Under these two modes, the existence of the reef ridge always decreases the bound LF wave amplitude and its ratio to the free LF wave amplitude inside the harbor, while its influences on the maximum LF wave amplitude and the free LF wave amplitude both depend on the reef-face slope.

Key words:

Harbor oscillations; Fringing-reef topography; Wave breaking; Bound low-frequency waves; Free low-frequency waves; FUNWAVE 2.0

* Corresponding author. E-mail: zhouli209@hotmail.com (L. Zhou).

1. Introduction

Low-frequency (LF) waves refer to the water waves with typical period scales between 30 s and 300 s and wavelength scales between 100 m and 10 km (Rabinovich, 2009). The LF waves can be produced and propagate underneath short wave groups through nonlinear wave interaction of short wave groups (Longuet-Higgins and Stewart, 1962). When the LF waves of certain frequencies propagate into a harbor, they can be trapped and significantly magnified inside the harbor, and eventually lead to large resonance of the free water surface (Bowers, 1977). This phenomenon is termed as harbor resonance or harbor oscillations. There are other external inducing factors that can also induce harbor resonance, such as shear flows (Fabrikant, 1995), fluctuations of atmospheric pressure and wind speed (De Jong and Battjes, 2004), impact waves emerging near the harbor (Gao et al., 2018c; Wang et al., 2011) and tsunamis originating from distant earthquakes (Gao et al., 2017a; Gao et al., 2016b; Gao et al., 2018a). However, for most ports and harbors in the world, the most common external inducing factor may be the LF waves mainly produced via nonlinear wave interaction of short wave groups. Through generating excessive ship movements, harbor resonance may disturb cargo loading/unloading, reduce operational efficiency and cause extremely large mooring forces which may break mooring lines (Kumar et al., 2016).

The effects of the LF waves on port operations of Gijón Port (Spain) were investigated by González-Marco et al. (2008), and it was found that the LF waves can remarkably increase the port's downtime. Numerous other numerical analyses and field observations on the LF waves in ports and harbors, such as Marina di Carrara harbor in Italy (Guerrini et al., 2014), Pohang New Harbor in South Korea (Kumar et al., 2014), Paradip Port in India (Kumar and Gulshan, 2017, 2018) and Two Rocks Marina in Australia (Thotagamuwage and Pattiaratchi, 2014a, b), have also affirmed the above-mentioned finding by uncovering strong relevance between short wave groups outside the harbor and the LF waves inside the harbor. Hence, to identify layouts and technical solutions that can minimize the downtime of the harbor, it is very essential to implement further investigations to improve our understanding of the LF wave climates inside the harbor during harbor oscillations.

Dong et al. (2013) proposed a LF wave analysis procedure to decouple the LF waves inside the harbor into free and bound LF waves. Subsequently, by using this wave analysis procedure and a fully nonlinear Boussinesq model FUNWAVE 2.0 (Kirby et al., 2003), Gao et al. (2016a) studied the influences of the incident short wave amplitude and the incident short wavelength on the free

and bound LF waves inside the harbor under the conditions of the lowest four resonant modes induced by bi-chromatic short wave groups. Subsequently, by employing another fully nonlinear Boussinesq model FUNWAVE-TVD (Shi et al., 2012), Gao et al. (2017a; 2018a) studied the transient harbor oscillations induced by N-waves and successive solitary waves. In Dong et al. (2013) and Gao et al. (2016a; 2017a; 2018a), the effects of offshore topography on the LF waves inside the harbor were not considered because the water depths in their studies were set to be constant. Recently, Gao et al. (2017b) and Gao et al. (2017c) further studied the effects of fringing reefs on free and bound LF waves and their relative components inside the harbor when the lowest five resonant modes were excited by bi-chromatic short wave groups. Because relatively small incident wave amplitudes were adopted in these two papers, wave breaking did not occur over the fringing reefs. More recently, considering that the wave-breaking phenomenon were observed frequently due to relatively shallow water depth over fringing reefs (Chen et al., 2018a; Chen et al., 2018b; Dong et al., 2014; Thotagamuwage and Pattiaratchi, 2014a, b; Yao et al., 2018), Gao et al. (2018b) further extended the studies of Gao et al. (2017b) to consider wave breaking over the reef by adopting the incident short wave amplitudes that were much larger than those in Gao et al. (2017b). However, the studies in Gao et al. (2018b) were only confined to the lowest resonant mode; the effects of the fringing reef on the LF wave climates inside the harbor for higher modes under the condition of wave breaking over the reef are still unknown.

To improve the knowledge of the LF waves involved in fringing reef topographies and harbor oscillations, this article further studies how the related LF wave parameters inside the harbor (including the maximum LF wave amplitude, the free and the bound LF waves and their relative components) vary with the topographic change of the fringing reef when wave breaking occurs over the reef. Compared to Gao et al. (2018b), there are mainly two study progresses. Firstly, to discuss the differences and similarities between different resonant modes, the related investigations are extended from the lowest mode in Gao et al. (2018b) to higher modes (i.e., the 2^{nd} to the 5^{th} modes) in this article. Secondly, the changing scope of the reef-face slope employed in this article is further expanded, compared with that utilized in Gao et al. (2018b). Identical to Gao et al. (2016a) and Gao et al. (2018b), all numerical simulations in this paper are carried out by using FUNWAVE 2.0 as well. For simplification, the harbor is assumed to be long and narrow, and then the free surface movement inside the harbor essentially becomes one-dimensional. The LF wave analysis procedure

proposed by Dong et al. (2013) is adopted to decouple the LF waves inside the harbor into free and bound LF waves.

The remainder of the paper is organized as follows: Section 2 briefly introduces the numerical model and the LF wave analysis procedure. Section 3 describes the setup of all numerical simulations and all wave parameters used in the simulations. Section 4 presents the simulation results, which are explained in detail. Main conclusions of this paper are drawn in Section 5.

2. Numerical model and LF wave analysis procedure

2.1. Numerical model

All numerical simulations in this paper are carried out by employing the famous and widespread FUNWAVE 2.0 model, which was proposed and developed by Kirby et al. (2003). The control equations of the model are based on the fully nonlinear Boussinesq equations derived by Wei et al. (1995). Subsequently, the control equations were discretized on the staggered grid in generalized curvilinear coordinates by Shi et al. (2001) to better fit irregularly shaped shorelines. The one-way wave-making method presented by Chawla and Kirby (2000) is utilized to produce monochromatic or random waves. To effectively absorb the energy of outgoing waves, sponge layers are deployed at the boundaries of the computational domain. Meanwhile, in order to consider the influences of bottom friction, wave breaking and sub-grid lateral turbulent mixing on the wave hydrodynamics, some additional terms are added to the momentum equation. The coefficients related to these additional terms include the bed friction coefficient f_b, two breaking-related parameters, C_{br} and δ_b, and the sub-grid mixing coefficient C_m, and all of them can be adjusted based on existing physical modeling experiments. The detailed definitions and explanations of the four coefficients can be referred to Kirby et al. (2003). The capacity of the model to simulate wave propagation and transformation from deep to shallow water has been well verified by physical experiments (Kirby et al., 2003; Ma et al., 2017).

To further validate the capability of FUNWAVE 2.0 to predict wave energy evolution and wave transformation over fringing reefs, Gao et al. (2018b) adopted the model to reproduce the physical experiments of Nwogu and Demirbilek (2010) that were performed in a 2D wave flume at the University of Michigan. The experiments considered a reef profile typical of fringing reef systems along the southeast coast of Guam. Gao et al. (2018b) compared the numerical results of the

significant wave height variation and the mean water level setup over the reef with the experimental data of Nwogu and Demirbilek (2010), and found that the values of f_b=0.0001, C_{br}=0.50, δ_b=1.25 and C_m=0.2 produce the best agreement between the numerical results and the experimental data. Identical to Gao et al. (2018b), the values of C_{br}=0.50, δ_b=1.25 and C_m=0.2 will be utilized in our simulations that will be elaborated in Section 3, and the bed friction coefficient f_b will be set to zero. The reason why f_b is set to zero is that this paper only studies the influences of the topographic changes of the fringing reef on the LF oscillations inside the harbor. The topographic changes of the reef include various reef-face slopes and whether the reef ridge exists or not. As stated by Gao et al. (2018b), if the bottom friction was considered in numerical simulations, the analysis results would be affected inevitably by the bottom friction, and would not be influenced purely by the topographic change of the reef.

2.2. LF wave analysis procedure

Identical to Gao et al. (2018b), the LF wave analysis procedure proposed by Dong et al. (2013) is employed in this paper to decouple the LF waves inside the harbor into free and bound LF waves. To facilitate the reader's understanding of the current study, the wave analysis procedure is described briefly in this section.

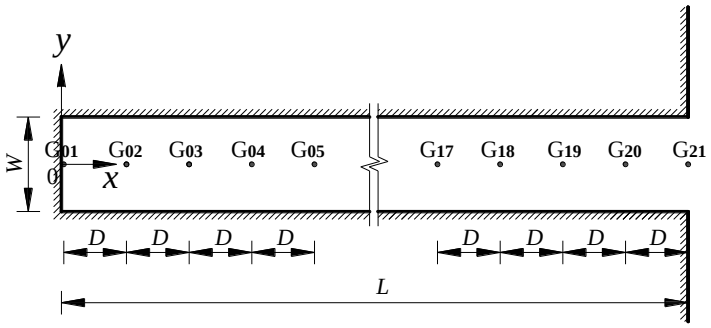

Fig. 1. Definition sketch of the harbor and the deployment of the wave gauges inside the harbor

Fig. 1 presents the sketch of the harbor utilized in the current study and the deployment of the wave gauges inside the harbor. The harbor has a width of W=5.0 m and a length of L=50.0 m. Twenty-one wave gauges (G_{01}–G_{21}) are equidistantly arranged along the center line of the harbor, with a spacing of D=2.5 m. The origin of the coordinate system (o, x, y, z) is located at the still water

level (SWL) with the z-axis measured upwards. The water depth inside the harbor is a constant, h_I=1.0 m. The gauges G_{01} and G_{21} are deployed at the inner end of the harbor and at the harbor entrance, respectively.

When the elongated harbor is exposed to bi-chromatic waves groups, all the wave components inside the harbor, including primary waves, second-order bound and free LF waves, take the form of standing waves. Due to the vertical fully-reflective wall at the inner end of the harbor, an antinode exists at x=0 for all the standing wave components. The LF component inside the harbor can be expressed theoretically as follows (Bowers, 1977):

$$\eta_{\mathrm{LF}}=\zeta_{\mathrm{b}}\cos[(2\pi\Delta f)t-\alpha_{\mathrm{b}}]\cos(\Delta kx)+\zeta_{\mathrm{f}}\cos[(2\pi\Delta f)t-\alpha_{\mathrm{f}}]\cos(\kappa x), \tag{1}$$

where $\Delta f=|f_1-f_2|$ and $\Delta k=|k_1-k_2|$. (f_1, k_1) and (f_2, k_2) denote the frequencies and wavenumbers of the primary waves and satisfy the linear dispersion relation. The first and second terms on the right-hand-side of Eq. (1) are the bound and free LF standing wave components, respectively. Δf and Δk correspond to the frequency and wavenumber of the bound LF waves. κ is the wavenumber of the free LF waves, and (κ, Δf) also satisfy the linear dispersion relation. ζ_{b} and ζ_{f} are the amplitudes of the bound and free LF waves, respectively, and α_{b} and α_{f} are their initial phases. g is the gravitational acceleration. Via some algebraic transformations, the squared amplitude of the LF component along the central line can be formulated as follows:

$$A_{\mathrm{LF}}(x)^2=a\varphi_0(x)+b\varphi_1(x)+c\varphi_2(x), \tag{2}$$

where

$$\begin{aligned}&a=\zeta_{\mathrm{b}}{}^2,\ b=\zeta_{\mathrm{f}}{}^2,\ c=2\zeta_{\mathrm{b}}\zeta_{\mathrm{f}}\cos(\alpha_{\mathrm{b}}-\alpha_{\mathrm{f}}),\\&\varphi_0(x)=\cos^2(\Delta kx),\ \varphi_1(x)=\cos^2(\kappa x),\ \varphi_2(x)=\cos(\Delta kx)\cos(\kappa x).\end{aligned} \tag{3}$$

The amplitudes of the LF component for all the wave gauges inside the harbor, $A_{\mathrm{LF}}(x_i)$ (i=1, 2,…, 21), can be obtained using the discrete Fourier transform for the free surface signals. x_i refers to the abscissa value of each wave gauge. Considering that $\varphi_0(x)$, $\varphi_1(x)$ and $\varphi_2(x)$ are linearly independent, the unknown variables a, b and c can be calculated by using the least squares method, and then the values of ζ_{b}, ζ_{f} and $|\alpha_{\mathrm{b}}-\alpha_{\mathrm{f}}|$ are naturally obtained. The capability of this wave analysis procedure to separate the bound and free LF waves inside the harbor under different resonant modes was fully examined in Dong et al. (2013) and Gao et al. (2016a).

3. Numerical setup

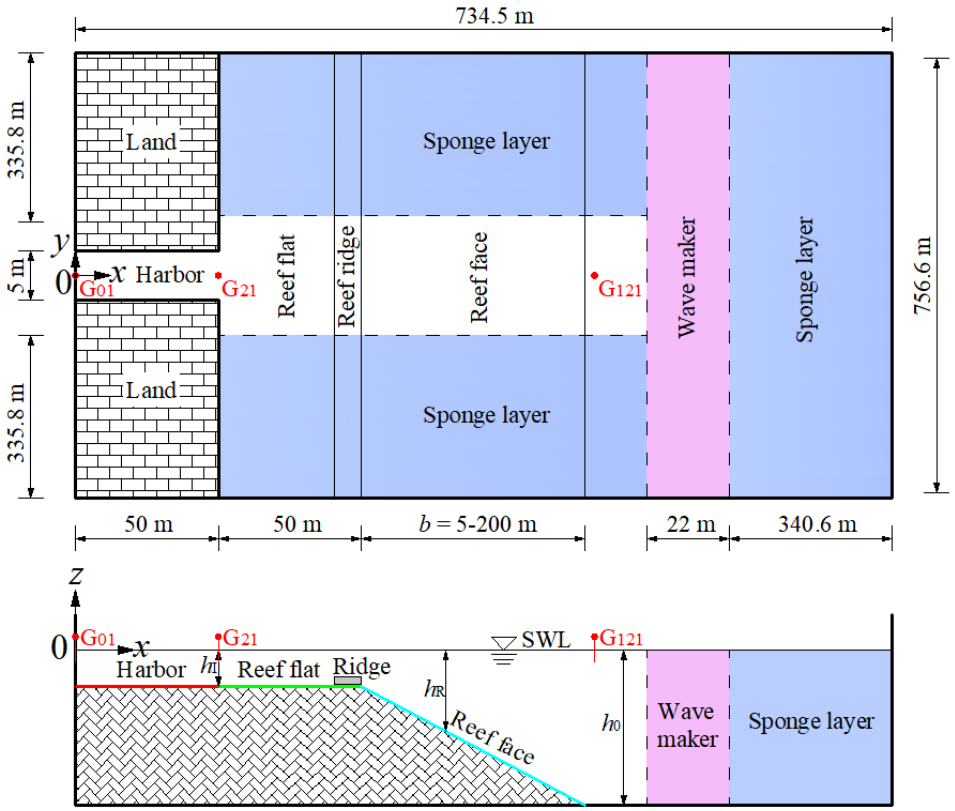

Fig. 2. Sketch of the numerical wave flume: (a) top view; (b) longitudinal section at y=0. Due to the symmetry of the flume with respect to the x-axis, only a half-domain (i.e. $y \geq 0$) is utilized for simulations.

Fig. 2 shows the numerical wave flume adopted in all simulations. The origin of the Cartesian coordinate system (o, x, y, z) is placed at the still water level with z-axis pointing upwards. The wave flume has dimensions of 734.5 m by 756.6 m. To facilitate comparing the results of higher modes with those of the lowest mode, the water depths inside the harbor, over the reef flat and at the open sea and the plane size of the harbor are set to be identical to those in Gao et al. (2018b). As described above, the harbor has dimensions of 50.0 m by 5.0 m. All the boundaries of the harbor and the wave flume are set to be fully reflective. The length of the reef flat that is located adjacent to the harbor entrance is 50.0 m. To more systematically investigate the effects of the reef-face slope on the LF waves inside the harbor, the changing range of the reef-face width, b, is expanded from 5.0 m – 100.0 m in Gao et al. (2018b) to 5.0 m – 200.0 m in an interval of 5.0 m. The still water depth over the reef flat and inside the harbor is h_1=1.0 m, and the still water depth over the open ocean is h_0=5.0

m. 121 wave gauges (G_{01}–G_{121}) are equidistantly deployed along the central line of the flume with a spacing of 2.5 m, among which the gauges G_{01}–G_{21} are placed inside the harbor. The abscissa values of the gauges G_{01}, G_{21} and G_{121} are x=0, 50.0 and 300.0 m, respectively. Besides, identical to Gao et al. (2018b), in order to discuss the influences of the reef ridge on the related LF wave parameters inside the harbor, two idealized fringing reef profiles are taken into consideration: (1) a reef with an idealized ridge and (2) a reef without a ridge. For the former profile, a rectangular box is placed on the reef flat with its front face aligned to the reef edge (x=100.0 m) to mimic an idealized ridge, and the dimensions of the box are 756.6 m by 6.0 m by 0.3 m. To guarantee the numerical stability, both the leeside and seaside vertical faces of the rectangular ridge are modified to a slope of S=0.6. To effectively dissipate the reflected and radiated waves, sponge layers with enough widths are deployed at the lower, upper and right boundaries of the numerical wave flume. In view of the geometric symmetry with respect to the x-axis, only half of the domain (i.e. $y \geq 0$) is utilized as the computational domain for all simulations so as to remarkably save the computational cost. Since FUNWAVE 2.0 is discretized using curvilinear grids, different grid sizes can be employed. In the x-axis direction, the grid size Δx is set to 0.5 m except in the sponge layer at the right boundary; the grid size Δx in the sponge layer gradually increases from 0.5 m to 10.2 m. In the y-axis direction, the grid size Δy gradually increases from 0.5 m inside the harbor to 6.7 m outside the harbor. A total simulation time of 1000.0 s and a time step of Δt=0.025 s are utilized in all simulations.

According to the analytical solution of the harbor resonance for the elongated rectangular harbor (Mei, 1983), Fig. 3 presents the amplification diagram of the linear long waves inside the harbor shown in Figs. 1 and 2. It can be seen that the lowest seven resonant frequencies are 0.014, 0.043, 0.073, 0.103, 0.133, 0.161, and 0.190 Hz, respectively. Considering that the amplification factors of the 6th and higher modes are very small (near to 1.0) and that the lowest mode has already been systematically studied in Gao et al. (2018b), only the harbor oscillations under the 2nd to the 5th modes induced by bi-chromatic short wave groups are investigated in this article (hereafter, the i^{th} resonant mode is referred to as "Mode i" for simplicity).

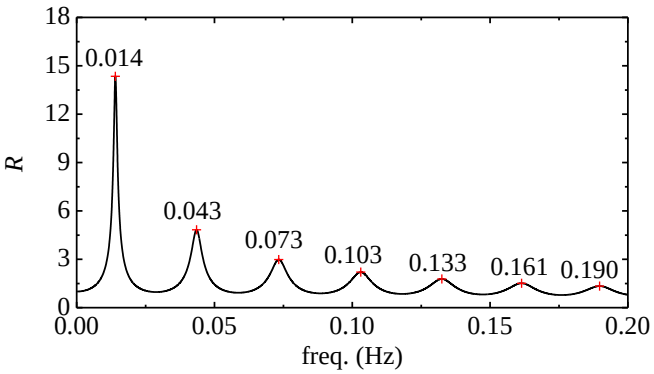

Fig. 3. Amplification factor, R, of the linear long waves for the harbor shown in Figs. 1 and 2 based on the analytical solution of Mei (1983). The numbers over the local maximum of the curve denote the corresponding resonant frequencies.

Table 1. Incident wave parameters for all cases in Modes 2−5. The amplitudes of the incident short waves, a_1=a_2=0.14 m, are used in all simulations, in which a_1 and a_2 denote the amplitudes of the incident f_1 and f_2 wave components, respectively.

Mode	f_1 (Hz)	f_2 (Hz)	f_0 (Hz)	h_0 / l_0	l_{lb} (m)	l_{0b} (m)	l_{lf} (m)	l_{0f} (m)
2	0.250	0.293	0.2715	0.236	62.6	77.5	72.7	161.8
3	0.250	0.323	0.2865	0.263	36.2	42.4	42.7	94.2
4	0.250	0.353	0.3015	0.291	25.2	28.0	30.2	65.6
5	0.250	0.383	0.3165	0.321	19.1	20.2	23.3	49.5

Table 1 presents the incident wave parameters for all cases in Modes 2-5. f_1 and f_2 in this table denote the frequencies of the incident bi-chromatic short waves. For all the four resonant modes, the value of f_1 is always set to 0.25 Hz, while the value of f_2 is determined based on the principle that the beat frequency, $\Delta f = |f_1 - f_2|$, corresponds to their respective resonant frequencies. $f_0 = (f_1 + f_2)/2$ denotes the average frequency of the incident bi-chromatic short waves. $l_0 = g/(2\pi f_0^2)$ denotes the average deep-water wavelengths of the incident short waves, and g is the gravitational acceleration. l_{lb} and l_{0b} denotes the wavelengths of the bound LF waves inside the harbor and at the open ocean, respectively. l_{lf} and l_{0f} refer to the wavelengths of the free LF waves inside the harbor and at the open ocean, respectively. By reference to Gao et al. (2018b) , the incident short wave amplitudes of a_1=a_2=0.14 m are adopted in all simulations to ensure the occurrence of wave breaking over the fringing reef, in which a_1 and a_2 denote the amplitudes of the

incident f_1 and f_2 wave components, respectively.

4. Results and discussion

4.1. Time series and wavelet analysis

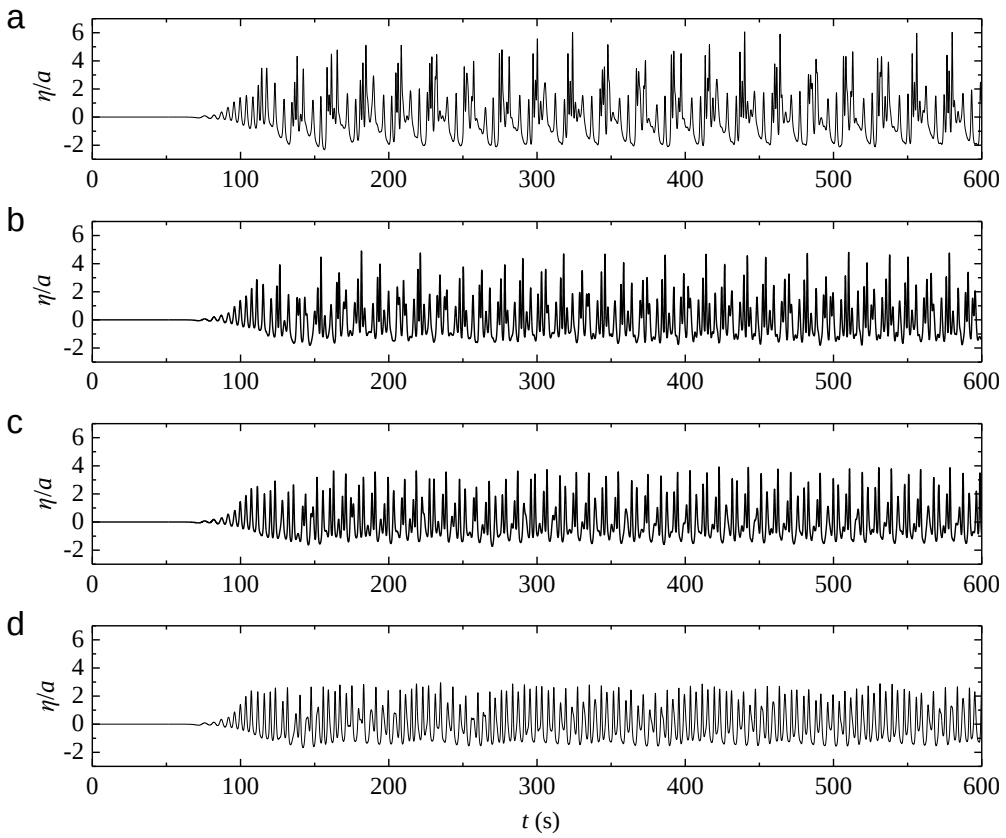

Fig. 4. Time histories of the free surface elevations at the gauge G_{01} for (a) Mode 2, (b) Mode 3, (c) Mode 4 and (d) Mode 5 under the conditions of b=100.0 m and without reef ridge, in which $a=\sqrt{a_1 a_2}$.

Fig. 4 illustrates the time histories of the free-surface elevations at the gauge G_{01} under the conditions of b=100.0 m and without reef ridge. It is noted that the free-surface elevations shown in this figure are non-dimensionlized by the average amplitude of the incident bi-chromatic short waves, $a=\sqrt{a_1 a_2}$. It is seen from Fig. 4 that the free surface inside the harbor is calm at the beginning period of the simulations, and for all the four cases, the incident short waves arrive at the location of the gauge G_{01} at around 80.0 s. By employing the Morlet wavelet transform technique

(Dong et al., 2008), the wavelet energy spectra of the free-surface elevations shown in Fig. 4 can be further obtained and are presented in Fig. 5. Based on these wavelet energy spectra, the variations of the wave energy in both the time and the frequency domains can be visually observed (Ma et al., 2011; Ma et al., 2010). It is seen that the LF components presents strong wave energy level for all the four cases, which is due to the fact that these LF components correspond to various resonant modes and hence are significantly amplified inside the harbor. Moreover, it is also observed that the energy of the short waves increases from zero to their maximum levels in very short time (about 50.0 s) and then maintains steady state until the end of the computation. While the LF waves need more time to reach the steady state from the initial response phase; the LF waves for all the four cases attain the steady state at about t=300.0 s. In this paper, only the steady-state processes (i.e., the free-surface signals from t=300.0 s to t=1000.0 s) are used to analyze the related wave parameters in all simulations. Through simple calculations, it is seen that for all the four resonant modes, the steady-state processes are at least 30 times the period of the LF waves, which is long enough to achieve reliable analysis results.

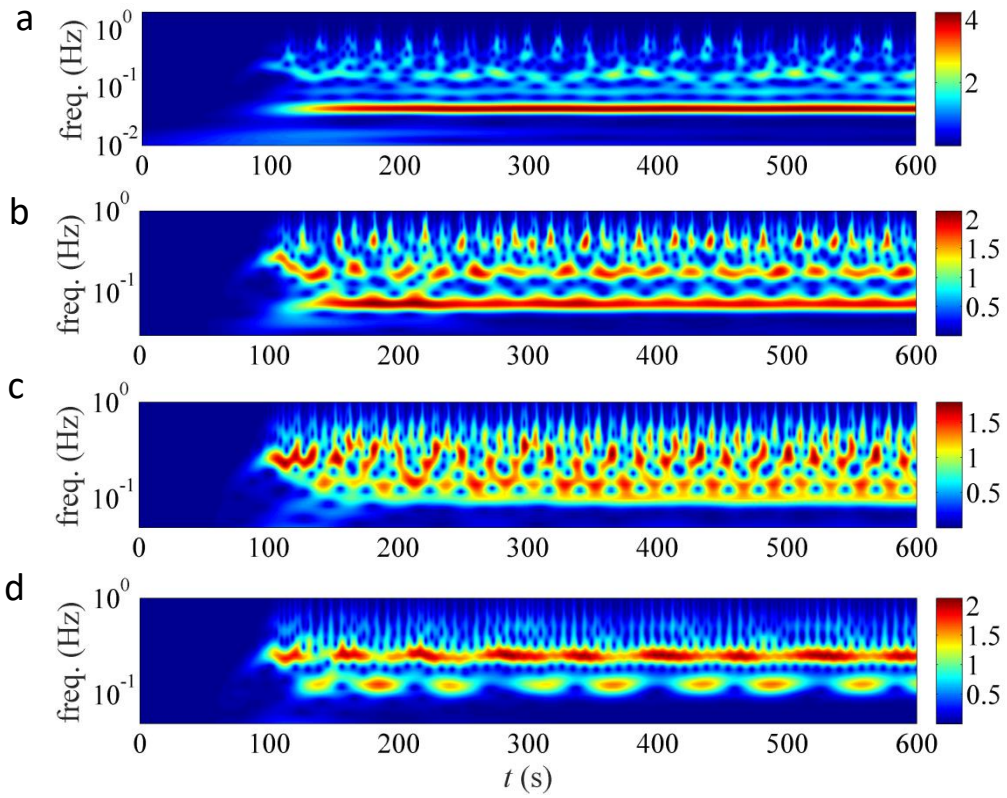

Fig. 5. Wavelet energy spectra at the gauge G_{01} for (a) Mode 2, (b) Mode 3, (c) Mode 4 and (d) Mode 5 under the conditions of b=100.0 m and without reef ridge

4.2. Wave amplitude evolutions of short waves and LF waves

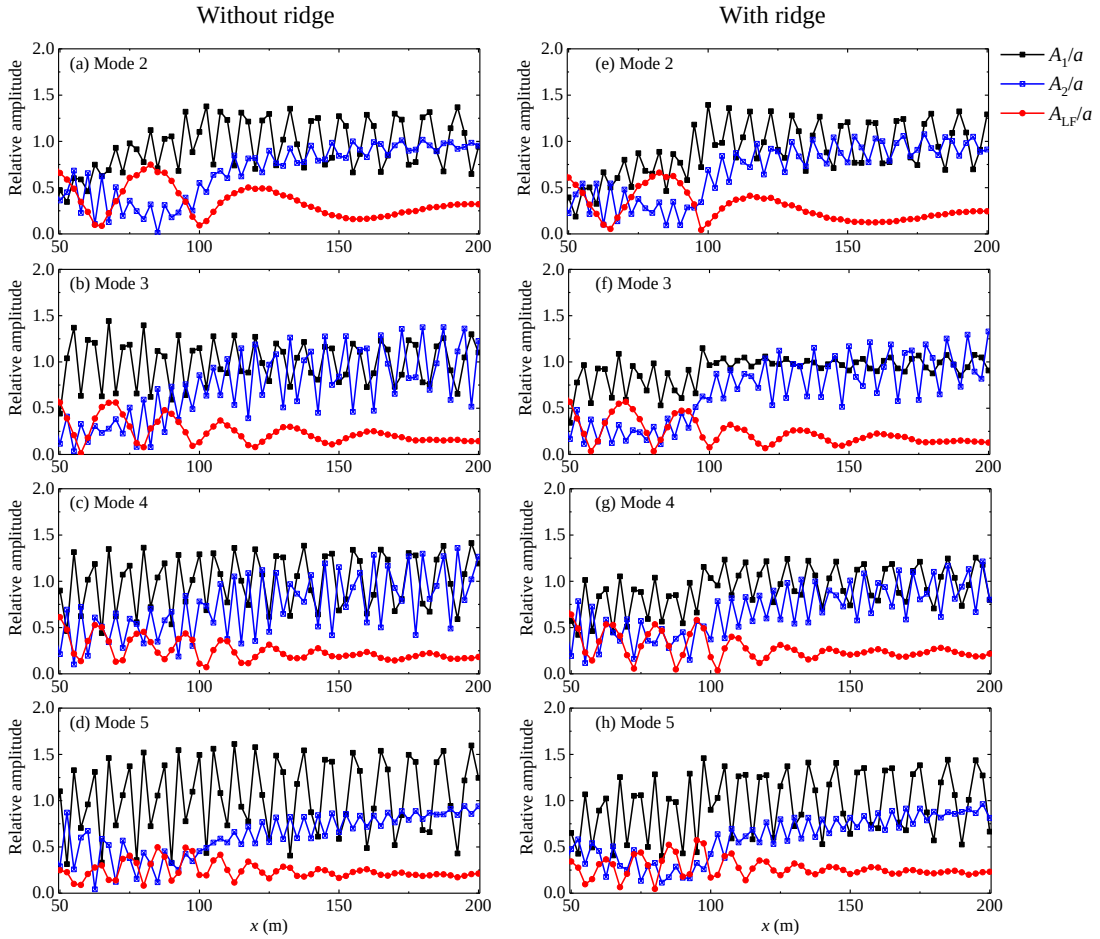

Fig. 6. Evolutions of the wave amplitudes of short waves and LF waves over the reef along the *x*-axis for various resonant modes under the condition of b=100.0 m. (a)–(d) correspond to the cases without the ridge, and (e)–(h) correspond to the cases with the ridge.

Before employing the LF wave analysis technique introduced in Section 2.2 to decouple the LF waves inside the harbor into free and bound LF waves, it is essential to check whether the wave-breaking phenomenon appears over the fringing reef for the incident short wave amplitudes employed in this article (i.e., a_1=a_2=0.14 m). Fig. 6 presents the evolutions of the wave amplitudes of both short waves and LF waves over the reef along the *x*-axis for various resonant modes under the condition of the reef-face width b=100.0 m. The amplitudes of various wave components shown in this figure are obtained by employing the discrete Fourier transform for the free surface signal of each wave gauge. When b=100.0 m, the reef flat, the reef face and the open ocean are respectively situated at the ranges of 50.0< $x \leq$ 100.0 m, 100.0< $x \leq$ 200.0 m and $x >$ 200.0 m. It can be obviously

observed from this figure that because of the wave energy reflection from the shoreline, both the short waves and the LF waves present the properties of standing waves for all the four modes considered in this article. For the short wave f_2 component amplitude A_2, there is always a significant and persistent decrease over the reef face along the inshore direction, no matter whether the reef ridge exists or not. For the short wave f_1 component amplitude A_1, there also exists a notable decline near the reef edge (x=100.0 m) along the inshore direction for Mode 2 without ridge and for all the four modes with ridge. In contrast, for all the eight cases shown in this figure, the LF wave amplitude A_{LF} trends to become more and more obvious over the fringing reef along the inshore direction, and the value of A_{LF} has approached or even exceeded the values of A_1 and A_2 at the shoreline (x=50.0 m). All these phenomena indicate that for all the four resonant modes, wave breaking always occurs over the reef face or near the reef edge under the condition of the incident short wave amplitudes employed in this article.

4.3. Effect of the reef-face slope on LF waves

Using the LF wave analysis procedure described in Section 2.2, the free and the bound LF wave components inside the harbor are decoupled for all the simulations. Fig. 7 shows the LF wave amplitudes at all the wave gauges inside the harbor and their fitted envelopes obtained by employing the LF wave analysis procedure for various resonant modes under the condition of b=100.0 m. It can be clearly observed that for all the eight cases, the fitted envelopes agree very well with the LF wave amplitudes at all the wave gauges inside the harbor. This indicates that the decoupling amplitudes of the free and the bound LF waves are precise and reliable. Table 2 lists the decoupling results of these eight cases. A_m in this table refers to the maximum LF wave amplitude inside the harbor. It should be noted that although A_m for the lowest resonant mode studied in Gao et al. (2018b) always appears at the inner end of the harbor where the gauge G_{01} is placed, it is not always true for higher modes. Among the eight cases, A_m for the two cases of Modes 3 and 4 without ridge corresponds to the LF wave amplitude at the gauges 19 and 20, respectively (see Fig. 7b and c). For all these eight cases, the values of ζ_b / ζ_f are all less than 100% although the magnitudes of ζ_b and ζ_f are different from each other. This indicates that for these eight cases, the bound LF waves are always weaker than the free LF waves inside the harbor.

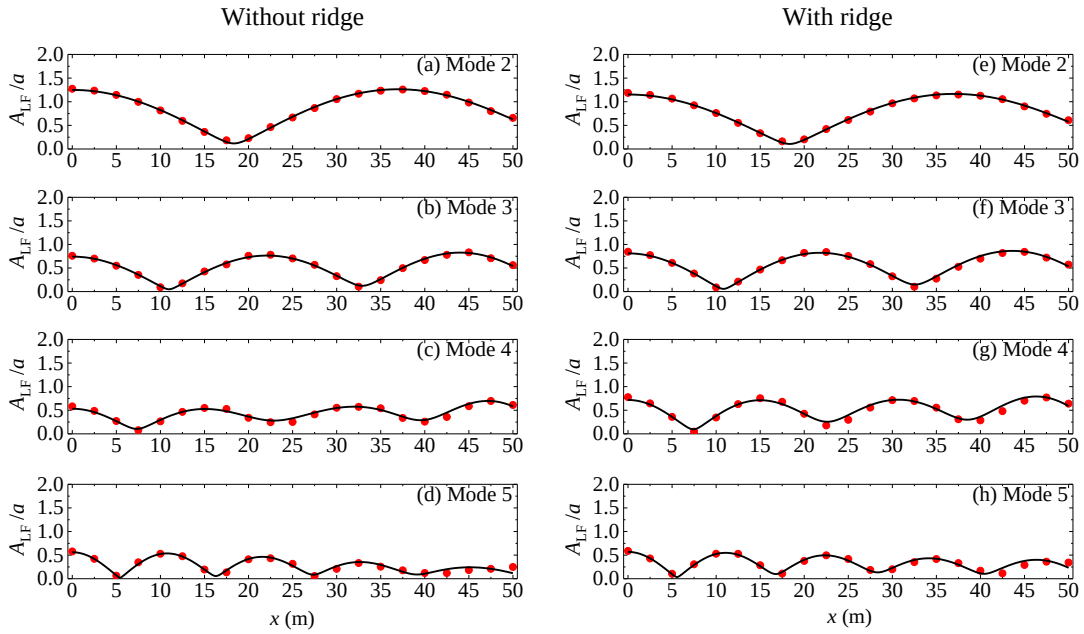

Fig. 7. The LF wave amplitudes (red dots) at all the wave gauges inside the harbor and their fitted envelopes (black lines) obtained by employing the wave analysis procedure for Modes 2–5 under the condition of b=100.0 m. (a)–(d) correspond to the cases without the ridge, and (e)–(h) correspond to the cases with the ridge.

Table 2. The decoupling results of the free and the bound LF waves for the eight cases shown in Fig. 7. A_m refers to the maximum LF wave amplitude inside the harbor. ζ_f and ζ_b refer to the amplitudes of the free and the bound LF waves, respectively, and α_f and α_b denote their respective initial phases.

Case	Results				
	A_m (m)	ζ_f (m)	ζ_b (m)	$\lvert\alpha_f-\alpha_b\rvert$ (°)	ζ_b/ζ_f (%)
(a)	1.78×10^{-1}	1.98×10^{-1}	6.67×10^{-2}	119.8	33.63
(b)	1.16×10^{-1}	1.22×10^{-1}	2.88×10^{-2}	135.1	23.59
(c)	9.75×10^{-2}	8.32×10^{-2}	4.89×10^{-2}	117.6	58.76
(d)	8.10×10^{-2}	5.27×10^{-2}	2.80×10^{-2}	27.81	53.06
(e)	1.66×10^{-1}	1.82×10^{-1}	6.04×10^{-2}	119.6	33.11
(f)	1.18×10^{-1}	1.26×10^{-1}	3.00×10^{-2}	121.5	23.77
(g)	1.09×10^{-1}	1.04×10^{-1}	4.45×10^{-2}	106.9	42.79
(h)	8.23×10^{-2}	6.48×10^{-2}	2.27×10^{-2}	56.56	35.02

Fig. 8 presents the variations of the maximum LF wave amplitude and the corresponding amplitudes of the free and the bound LF waves inside the harbor with respect to the slope coefficient, S^{-1}, for all the cases in Modes 2−5. The following three phenomena can be clearly observed from this figure. Firstly, for all the four modes studied in this article, in general, all of the maximum LF wave amplitude, the free and the bound LF wave amplitudes inside the harbor widely fluctuate with respect to the reef-face slope, which is different from the finding for the lowest mode in Gao et al. (2018b) that all these three variables increase monotonously with the increasing of the reef-face slope. Secondly, the two fluctuating curves of the maximum LF wave amplitude and the free LF wave amplitudes are almost paralleled with each other, no matter whether the reef ridge exists or not. It coincides with the related finding in Gao et al. (2017c). Thirdly, for all the cases in Modes 2−4, the free LF waves inside the harbor are always significantly larger than the corresponding bound LF waves. This is because the free LF waves in these three modes have relatively large amplification factors and are remarkably magnified inside the harbor (see Fig. 3). While for the cases in Mode 5, although the free LF waves inside the harbor still tend to be larger than the bound LF waves overall, the difference between them becomes much smaller than those in Modes 2–4. For those cases at the range of $37.50 \le S^{-1} \le 41.25$ in Mode 5 and without ridge, the amplitude of the bound LF waves even slightly exceeds that of the free LF waves. This is mainly due to the fact that the free LF waves in Mode 5 have relatively small amplification factor (only about 1.79), and the magnifying effect of the harbor on the free LF waves inside the harbor is relatively limited.

Fig. 9 illustrates the variations of the amplitude ratios, ζ_b / ζ_f, with respect to the slope coefficient, S^{-1}, for all the cases in Modes 2−5. Similar to the three variables shown in Fig. 8, the amplitude ratios, ζ_b/ζ_f, inside the harbor also show wide fluctuations with the reef-face slope for all the four modes studied in this paper. Besides, in general, the values of ζ_b / ζ_f in Modes 4 and 5 are larger than those of ζ_b / ζ_f in Modes 2 and 3. For the cases without ridge (Fig. 9a), the values of ζ_b / ζ_f in Modes 4 and 5 fluctuate in the ranges of 41.8−66.5% and 48.1−108.3%, respectively, while the values of ζ_b / ζ_f in Modes 2 and 3 vary only in the ranges of 14.0−34.5% and 22.3−33.3%, respectively. For the cases with ridge (Fig. 9b), all the amplitude ratios in Mode 4 and most of the amplitude ratios in Mode 5 are also larger than the corresponding amplitude ratios in Modes 2 and 3. In addition, it also can be seen that the variation ranges of the amplitude ratio in Mode 5 are notably larger than those in the other three modes, no matter whether the ridge exists or

not. This also can be attributed to that the free LF waves in Mode 5 have relatively small amplification factor, and their amplification inside the harbor is very limited, which causes that the relative component of the free and the bound LF waves inside the harbor becomes more sensitive to the reef-face slope.

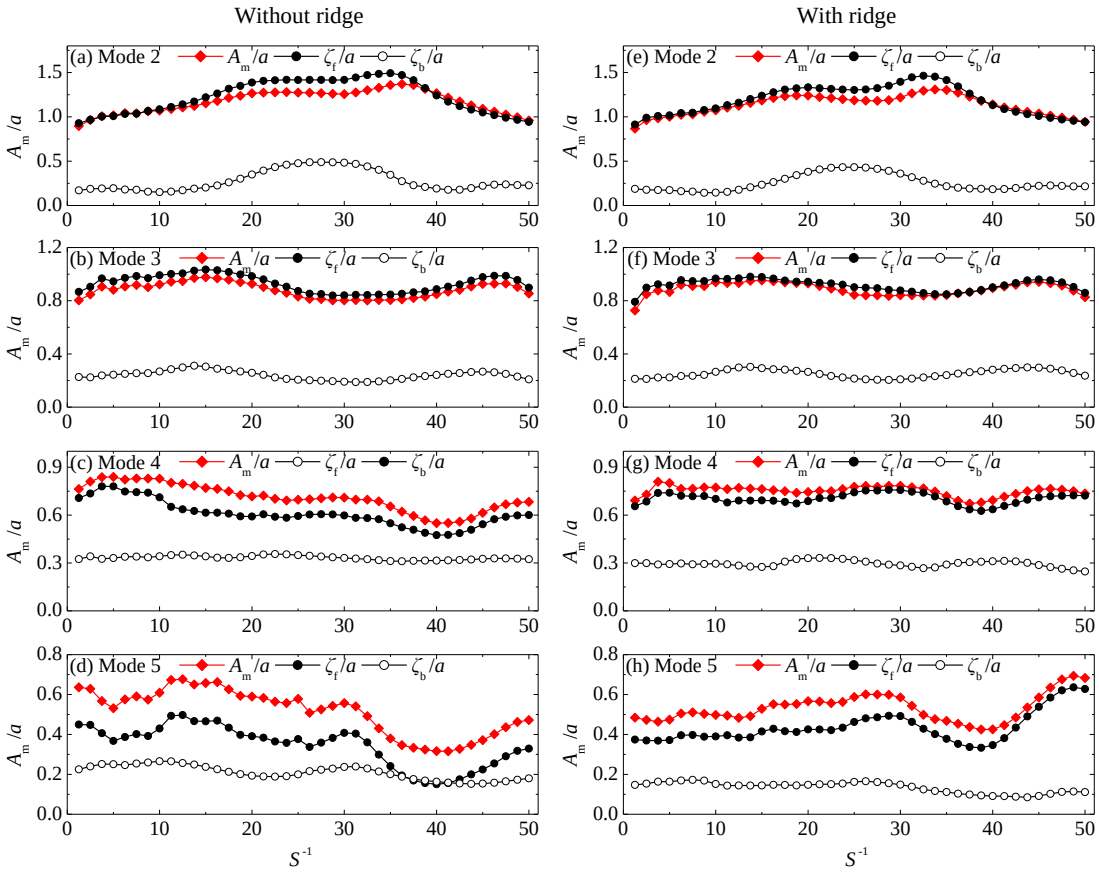

Fig. 8. Variations of the maximum LF wave amplitude and the corresponding amplitudes of the free and the bound LF waves inside the harbor with respect to the slope coefficient, S^{-1}, for all the cases in Modes 2–5. (a)–(d) correspond to the cases without the ridge, and (e)–(h) correspond to the cases with the ridge.

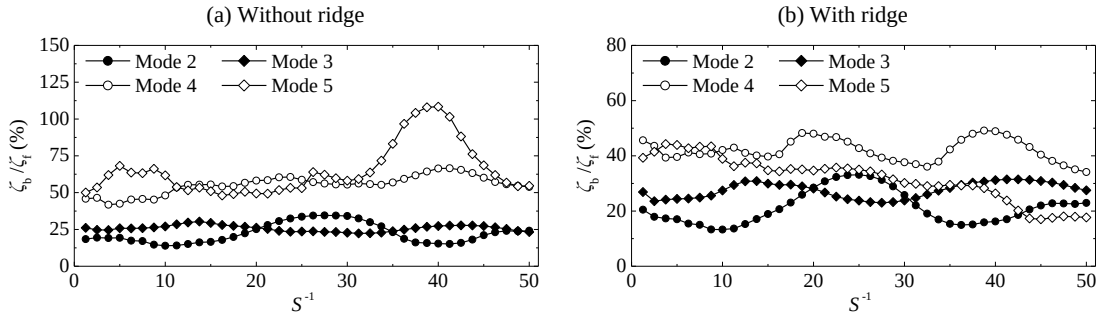

Fig. 9. The amplitude ratios, ζ_b/ζ_f, for all the cases in Modes 2–5. (a) and (b) correspond to the cases without and with the reef ridge, respectively.

4.4. Effect of the reef ridge on LF waves

Fig. 10 presents the comparison of the maximum LF wave amplitudes, A_m, under the two conditions of with and without reef ridge for Modes 2–5. It is seen that for Modes 2 and 3 (Fig. 10a and b), the maximum LF wave amplitude inside the harbor seems insensitive to the existence of the ridge. While for Modes 4 and 5 (Fig. 10c and d), the influence of the reef ridge on A_m depends on the reef-face slope. In both the two modes, when the reef-face slope, S, is large, the existence of the reef ridge tends to restrain the maximum LF wave amplitude inside the harbor. However, with the decreasing of the reef-face slope, the existence of the reef ridge gradually tends to enhance the maximum LF wave amplitude inside the harbor.

Fig. 11 shows the comparison of the free LF wave amplitudes, ζ_f, under the two conditions of with and without reef ridge for Modes 2–5. In general, all the phenomena presented in this figure are similar to those shown in Fig. 10. For Modes 2 and 3 (Fig. 11a and b), the free LF wave amplitude inside the harbor seems insensitive to the existence of the ridge. While for Modes 4 and 5 (Fig. 11c and d), when the reef-face slope is large, the existence of the reef ridge tends to restrain the free LF wave amplitude; with the decreasing of the reef-face slope, the existence of the reef ridge gradually tends to enhance it. Besides, by comparing Fig. 11c and d with the corresponding subgraphs in Fig. 10, it also can be seen that for both Modes 4 and 5, the ranges of the reef-face slope at which the free LF wave amplitude is intensified due to the existence of the reef ridge are obviously larger than those at which the maximum LF wave amplitude is strengthened due to the same reason.

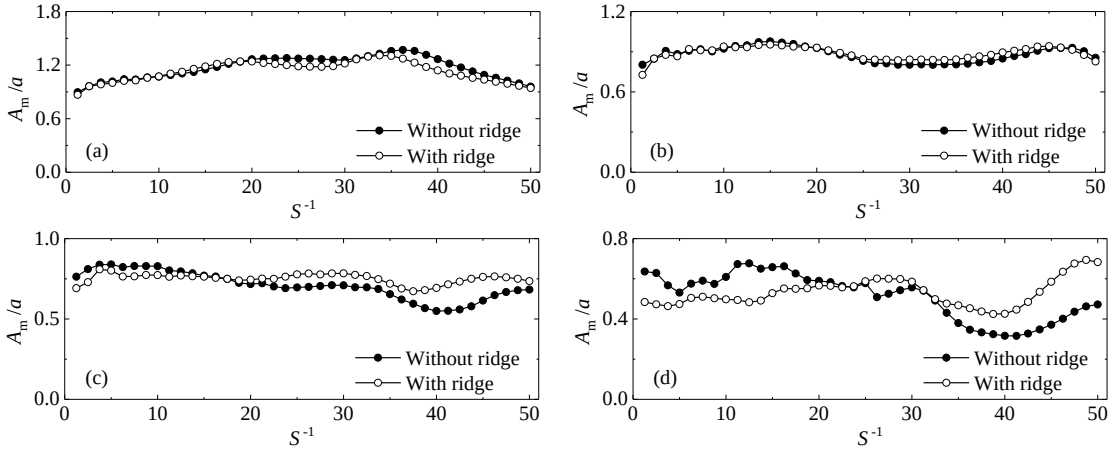

Fig. 10. Comparison of the maximum LF wave amplitudes, A_m, under the two conditions of with and without reef ridge. (a)–(d) correspond to Modes 2-5, respectively.

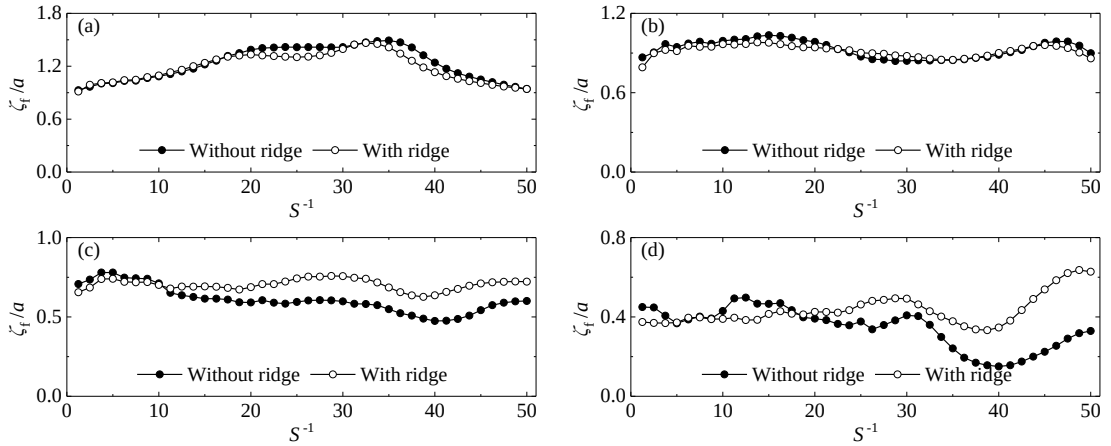

Fig. 11. Comparison of the free LF wave amplitudes, ζ_f, under the two conditions of with and without reef ridge. (a)–(d) correspond to Modes 2-5, respectively.

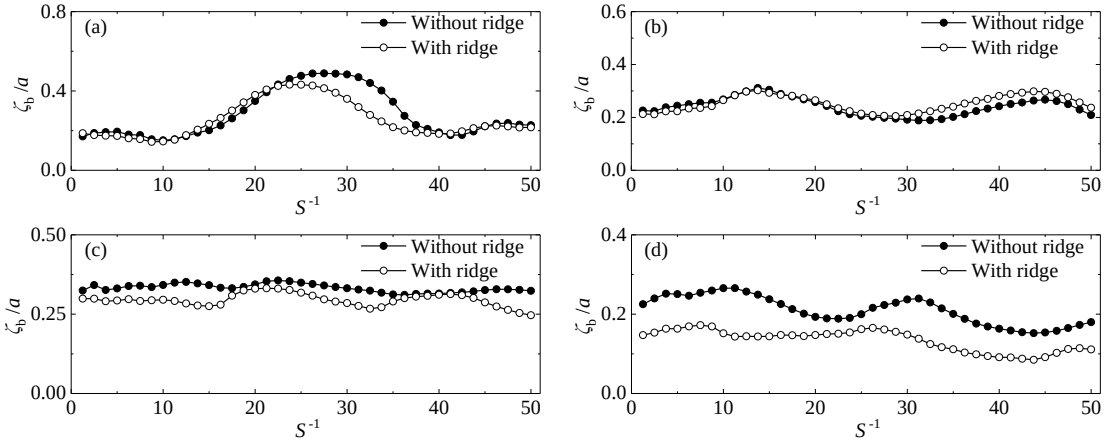

Fig. 12. Comparison of the bound LF wave amplitudes, ζ_b, under the two conditions of with and without reef ridge. (a)–(d) correspond to Modes 2-5, respectively.

Fig. 12 illustrates the comparison of the bound LF wave amplitudes, ζ_b, under the two conditions of with and without reef ridge for Modes 2–5. For both Modes 2 and 3 (Fig. 12a and b), it can be seen that for the vast majority of the reef-face slopes considered in this paper, the values of ζ_b under these two conditions are almost identical or very close to each other. In general, the bound LF wave amplitudes for these two modes are not very sensitive to the existence of the reef ridge. While for both Modes 4 and 5 (Fig. 12c and d), the existence of the reef ridge restrains the bound LF waves inside the harbor to some extent at the whole range of the reef-face slope considered in the paper, and the declining degree of the bound LF waves due to the existence of the ridge in Mode 5 is more obvious than that in Mode 4.

Finally, the comparison of the amplitude ratios, ζ_b/ζ_f, under the two conditions of with and without reef ridge for Modes 2-5 is presented in Fig. 13. The phenomena reflected in this figure are very similar to those embodied in Fig. 12. Specifically, for both Modes 2 and 3 (Fig. 13a and b), the influence of the reef ridge on the amplitude ratio seems very limited, overall; the values of ζ_b/ζ_f under these two conditions are almost identical or very close to each other for most of the reef-face slopes studies in this article. However, for both Modes 4 and 5 (Fig. 13c and d), the existence of the reef ridge obviously decreases the amplitude ratio at the whole range of the reef-face slope studies in this article, especially for the reef face with relatively small slope.

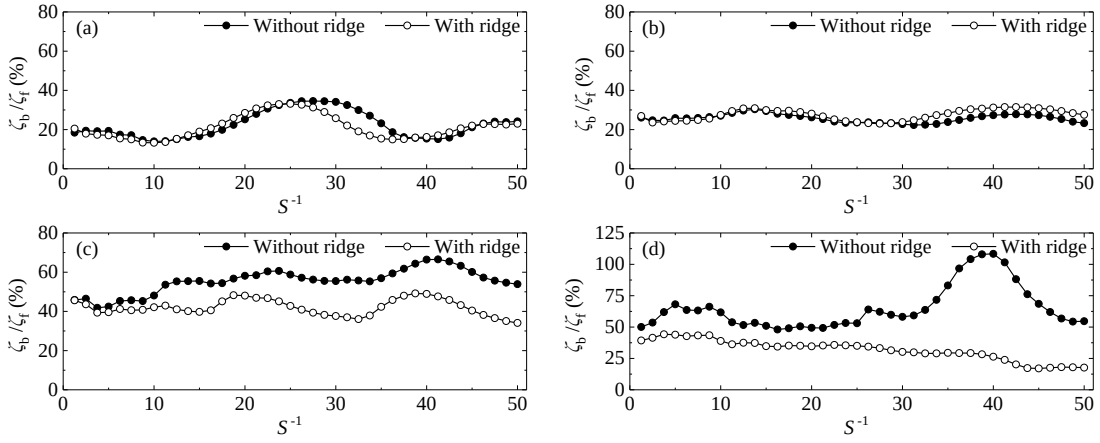

Fig. 13. Comparison of the amplitude ratios, ζ_b/ζ_f, under the two conditions of with and without reef ridge. (a)–(d) correspond to Modes 2-5, respectively.

5. Conclusions

The LF oscillations inside an elongated harbor near the fringing reef induced by bi-chromatic short wave groups are simulated by using FUNWAVE 2.0. The LF wave analysis procedure proposed by Dong et al. (2013) is utilized to decouple the LF waves inside the harbor into the free and the bound LF waves. Influences of the reef-face slope and the existence of the reef ridge on the maximum LF wave amplitude, the free and the bound LF waves and their relative components inside the harbor under the condition of wave breaking over the reef are comprehensively investigated. Although similar investigations have been carried out in Gao et al. (2018b), the previous studies were only confined to the lowest resonant mode. While in this article, the investigations on the effects of the fringing reef on the LF wave climates inside the harbor are extended to the higher resonant modes, i.e., Modes 2-5. The results of this study will enhance the knowledge of LF waves inside harbors involved in fringing reef topographies and harbor oscillations excited by the short wave groups.

The following conclusions can be drawn from the results of the current investigation:

1. For all the resonant modes considered in this paper, all the four above-mentioned variables (i.e., the maximum LF wave amplitude, the free and the bound LF waves and their relative components) present wide fluctuations with respect to the reef-face slope. The variation trends of the maximum LF wave amplitude and the free LF wave amplitude with respect to the reef-face slope are almost identical with each other for all the four modes, no matter whether the reef ridge exists or not. Besides, in general, the amplitude ratios of the bound and the free LF waves, ζ_b / ζ_f, in Modes 4 and 5 are shown to be larger than those in Modes 2 and 3, especially under the condition of without reef ridge.
2. The effects of the reef ridge on the LF wave climates inside the harbor for Modes 2 and 3 seem to be very limited. However, for Modes 4 and 5, its influences on the LF waves inside the harbor are obvious. For the latter two modes, the existence of the reef ridge always decreases the bound LF wave amplitude and the amplitude ratio, ζ_b / ζ_f, inside the harbor, while its influences on the maximum LF wave amplitude and the free LF wave amplitude both depend on the reef-face slope. When the reef-face slope is large, the existence of the reef ridge tends to restrain both the maximum LF wave amplitude and the free LF wave amplitude. However, with the decreasing of the reef-face slope, the existence of the reef ridge gradually tends to enhance these two

variables.

Finally, we reaffirm here that these conclusions are only valid for the given harbor and reef ridge, the incident short wave amplitudes and the variation range of the reef-face slope studied in this paper.

Acknowledgments

This work was financially supported by the National Natural Science Foundation of China (Grant Nos. 51609108 and 51809039), the Science Foundation from the Education Department of China Jilin Province (Grant No.JJKH20180452KJ) and the Jiangsu Government Scholarship for Overseas Studies (awarded to Dr. Junliang Gao for study abroad at the University of Bath).

References

Bowers, E.C., 1977. Harbour resonance due to set-down beneath wave groups. Journal of Fluid Mechanics 79, 71-92.

Chawla, A., Kirby, J.T., 2000. A source function method for generation of waves on currents in Boussinesq models. Applied Ocean Research 22 (2), 75-83.

Chen, H., Tang, X., Gao, J., Fan, G., 2018a. Parameterization of geometric characteristics for extreme waves in shallow water. Ocean Engineering 156, 61-71.

Chen, H., Tang, X., Zhang, R., Gao, J., 2018b. Effect of bottom slope on the nonlinear triad interactions in shallow water. Ocean Dynamics 68 (4-5), 469-483.

De Jong, M.P.C., Battjes, J.A., 2004. Seiche characteristics of Rotterdam Harbour. Coastal Engineering 51 (5-6), 373-386.

Dong, G.-H., Ma, Y.-X., Ma, X.-Z., 2008. Cross-shore variations of wave groupiness by wavelet transform. Ocean Engineering 35 (7), 676-684.

Dong, G., Chen, H., Ma, Y., 2014. Parameterization of nonlinear shallow water waves over sloping bottoms. Coastal Engineering 94, 23-32.

Dong, G., Gao, J., Ma, X., Wang, G., Ma, Y., 2013. Numerical study of low-frequency waves during harbor resonance. Ocean Engineering 68, 38-46.

Fabrikant, A.L., 1995. Harbor oscillations generated by shear flow. Journal of Fluid Mechanics 282, 203-217.

Gao, J., Ji, C., Gaidai, O., Liu, Y., 2016a. Numerical study of infragravity waves amplification during harbor resonance. Ocean Engineering 116, 90-100.

Gao, J., Ji, C., Gaidai, O., Liu, Y., Ma, X., 2017a. Numerical investigation of transient harbor oscillations induced by N-waves. Coastal Engineering 125, 119-131.

Gao, J., Ji, C., Liu, Y., Gaidai, O., Ma, X., Liu, Z., 2016b. Numerical study on transient harbor oscillations induced by solitary waves. Ocean Engineering 126, 467-480.

Gao, J., Ji, C., Liu, Y., Ma, X., Gaidai, O., 2017b. Influence of offshore topography on the amplification of infragravity oscillations within a harbor. Applied Ocean Research 65, 129-141.

Gao, J., Ji, C., Liu, Y., Ma, X., Gaidai, O., 2018a. Numerical study on transient harbor oscillations induced by successive solitary waves. Ocean Dynamics 68 (2), 193-209.

Gao, J., Ji, C., Ma, X., Liu, Y., Gaidai, O., 2017c. Numerical investigation of infragravity wave amplifications during harbor oscillations influenced by variable offshore topography. Ocean Dynamics 67 (9), 1151-1162.

Gao, J., Zhou, X., Zang, J., Chen, Q., Zhou, L., 2018b. Influence of offshore fringing reefs on infragravity period oscillations within a harbor. Ocean Engineering 158, 286-298.

Gao, J., Zhou, X., Zhou, L., Zang, J., Chen, Q., Ding, H., 2018c. Numerical study of harbor oscillations induced by water surface disturbances within harbors of constant depth. Ocean Dynamics 68 (12), 1663–1681.

González-Marco, D., Sierra, J.P., Ybarra, O.F.d., Sánchez-Arcilla, A., 2008. Implications of long waves in harbor management: The Gijón port case study. Ocean & Coastal Management 51 (2), 180-201.

Guerrini, M., Bellotti, G., Fan, Y., Franco, L., 2014. Numerical modelling of long waves amplification at Marina di Carrara Harbour. Applied Ocean Research 48, 322-330.

Kirby, J.T., Long, W., Shi, F., 2003. Funwave 2.0 Fully Nonlinear Boussinesq Wave Model On Curvilinear Coordinates. Report No. CACR-02-xx. Center for Applied Coastal Research, Dept. of Civil & Environmental Engineering, University of Delaware, Newark, Delaware.

Kumar, P., Gulshan, 2017. Extreme wave-induced oscillation in Paradip Port under the resonance conditions. Pure and Applied Geophysics 174 (2), 4501-4516.

Kumar, P., Gulshan, 2018. Theoretical analysis of extreme wave oscillation in Paradip Port using a 3-D boundary element method. Ocean Engineering 164, 13-22.

Kumar, P., Zhang, H., Kim, K.I., 2014. Spectral Density Analysis for Wave Characteristics in Pohang New Harbor. Pure and Applied Geophysics 171, 1169-1185.

Kumar, P., Zhang, H., Kim, K.I., Yuen, D.A., 2016. Modeling wave and spectral characteristics of moored ship motion in Pohang New Harbor under the resonance conditions. Ocean Engineering 119, 101-113.

Longuet-Higgins, M.S., Stewart, R.W., 1962. Radiation stress and mass transport in gravity waves, with application to 'surf beat'. Journal of Fluid Mechanics 13 (4), 481-504

Ma, Y., Chen, H., Ma, X., Dong, G., 2017. A numerical investigation on nonlinear transformation of obliquely incident random waves on plane sloping bottoms. Coastal Engineering 130, 65-84.

Ma, Y., Dong, G., Ma, X., 2011. Separation of obliquely incident and reflected irregular waves by the Morlet wavelet transform. Coastal Engineering 58 (8), 761-766.

Ma, Y., Dong, G., Ma, X., Wang, G., 2010. A new method for separation of 2D incident and reflected waves by the Morlet wavelet transform. Coastal Engineering 57 (6), 597-603.

Mei, C.C., 1983. The Applied Dynamics of Ocean Surface Waves. Wiley, New York.

Nwogu, O., Demirbilek, Z., 2010. Infragravity wave motions and runup over shallow fringing reefs. Journal of Waterway, Port, Coastal, and Ocean Engineering 136 (6), 295-305.

Rabinovich, A.B., 2009. Seiches and harbor oscillations, in: Kim, Y. (Ed.), Handbook of Coastal and Ocean Engineering. World Scientific Publishing, Singapore, pp. 193-236.

Shi, F., Dalrymple, R.A., Kirby, J.T., Chen, Q., Kennedy, A., 2001. A fully nonlinear Boussinesq model in generalized curvilinear coordinates. Coastal Engineering 42, 337-358.

Shi, F., Kirby, J.T., Harris, J.C., Geiman, J.D., Grilli, S.T., 2012. A high-order adaptive time-stepping TVD solver for Boussinesq modeling of breaking waves and coastal inundation. Ocean Modelling 43-44, 36-51.

Thotagamuwage, D.T., Pattiaratchi, C.B., 2014a. Influence of offshore topography on infragravity period oscillations in Two Rocks Marina, Western Australia. Coastal Engineering 91, 220-230.

Thotagamuwage, D.T., Pattiaratchi, C.B., 2014b. Observations of infragravity period oscillations in a small marina. Ocean Engineering 88, 435-445.

Wang, G., Dong, G., Perlin, M., Ma, X., Ma, Y., 2011. Numerical investigation of oscillations within a harbor of constant slope induced by seafloor movements. Ocean Engineering 38 (17-18), 2151-2161.

Wei, G., Kirby, J.T., Grilli, S.T., Subramanya, R., 1995. A fully nonlinear Boussinesq model for surface waves. Part 1. Highly nonlinear unsteady waves. Journal of Fluid Mechanics 294, 71-92.

Yao, Y., He, F., Tang, Z., Liu, Z., 2018. A study of tsunami-like solitary wave transformation and run-up over fringing reefs. Ocean Engineering 149, 142-155.